

DUST DESTRUCTION IN NON-RADIATIVE SHOCKS

H. ZHU^{1,2}, P. SLANE², J. RAYMOND², W.W. TIAN^{1,3,4}

¹Key Laboratory of Optical Astronomy, National Astronomical Observatories, Chinese Academy of Sciences, Beijing 100012, China; zhuhui@bao.ac.cn, tww@bao.ac.cn

²Harvard-Smithsonian Center for Astrophysics, 60 Garden Street, Cambridge, MA 02138, USA; pslane@cfa.harvard.edu, jraymond@cfa.harvard.edu

³School of Astronomy and Space Science, University of Chinese Academy of Sciences, Beijing 100049, China and

⁴Department of Physics and Astronomy, University of Calgary, Calgary, Alberta T2N 1N4, Canada

Draft version July 30, 2019

ABSTRACT

Supernova remnant (SNR) shock waves are the main place where interstellar dust grains are destroyed. However, the dust destruction efficiency in non-radiative shocks is still not well known. One way to estimate the fraction of dust destroyed is to compare the difference between postshock gas abundances and preshock medium total abundances when the preshock elemental depletion factors are known. We compare the postshock gas abundances of 16 SNRs in Large Magellanic Cloud (LMC) with the LMC interstellar medium abundances that we derived based on 69 slow-rotating early B-type stars. We find that, on average, $\sim 61\%$ of Si rich dust grains are destroyed in the shock while the fraction of dust destroyed is only $\sim 40\%$ for Fe rich dust grains. This result supports the idea that the high depletion of Fe in the diffuse neutral medium is not caused by the resilience of Fe rich grains but because of faster growth rate. This work also presents a potential way to constrain the chemical composition of interstellar dust.

Subject headings: dust, ISM: supernova remnants, ISM: abundance)

1. INTRODUCTION

Interstellar dust is a fundamental component of galaxies (Draine 2011). It modulates the spectra of galaxies by absorbing short wavelength radiation and re-radiating the energy in the infrared band. The thermal emission of dust could be an important cooling mechanism of collapsing dense molecular clouds, allowing star formation to occur. Dust also provides the formation site of H₂ molecules and shields molecules from ultraviolet radiation, which makes it central to interstellar gas chemistry. Dust even plays a critical role in controlling the temperature of the diffuse interstellar medium (ISM) by locking heavy elements inside it and ejecting photoelectrons into the gas.

It has been confirmed that dust can form: 1) in the ejecta of supernovae; 2) in the outflows of evolved stars (e.g. the red giant stars, carbon stars, planetary nebulae), and 3) through regrowth in the ISM. The first formation route is considered as an explanation for large amounts of dust seen in high redshift galaxies (e.g., Mailiano et al. 2004; Dwek et al. 2007; Valiante et al. 2009; Gall et al. 2011), while the second route contributes dust only to “present-day” galaxies which are old enough for low and intermediate mass stars to leave the main sequence (e.g., Draine 2003). Usually, dust from these two routes is called stardust. Technically, the regrowth route should work for any galaxies with sufficiently high densities to allow metal elements to accrete onto dust grain surfaces. The unsolved question is how much dust is from the regrowth process (e.g., Draine 2009; Dwek & Cherchneff 2011; Temim et al. 2015; Slavin et al. 2015). Studying dust destruction in the shocks of supernova remnants (SNRs) could help approach this issue because any imbalance between dust

formation of the first two routes and dust destruction from SNR shock waves will necessitate dust regrowth in the ISM. For example, a higher dust destruction rate will bring into question the ejecta of supernovae as the main dust formation site of high redshift galaxies and support the idea that supernovae may only provide the dust seeds to grow in the ISM.

During the past few decades, numerous studies have been done on dust destruction in shocks (e.g., Shull 1977; Draine & Salpeter 1979; McKee et al. 1987; Dwek et al. 1996; Jones et al. 1996; Williams et al. 2006; Borkowski et al. 2006; Raymond et al. 2013; Bochico et al. 2014; Slavin et al. 2015; Lakićević et al. 2015; Dopita et al. 2016, 2018). Previous studies suggested that dust destruction is usually caused by thermal/non-thermal sputtering, shattering and vaporization. Sputtering dominates over other processes in fast non-radiative shocks. The main processes are non-thermal sputtering and shattering in slow radiative shocks. However, the rate of dust destruction is still poorly known. Table 1 lists the measured fraction of dust destroyed in several SNRs in the Milky Way and Large Magellanic Cloud (LMC). As can be seen, the fraction of dust destroyed in non-radiative shocks varies from $\sim 20\%$ to $\sim 50\%$ with an averaged value of 34%. For radiative shocks, it could rise to more than 50% (Dopita et al. 2016, 2018). Compared with the recent numerical hydrodynamical model of Slavin et al. (2015), the measured fraction of dust destroyed in non-radiative shocks is lower than the prediction (see their Figure 7).

In this paper, we measure an averaged fraction of dust destroyed by non-radiative shocks based on the postshock gas abundances of 16 LMC SNRs. We then

apply the result to constrain recent dust models. In section 2, we describe the general concept and equation to calculate the fraction of dust destroyed. In section 3, we show how to obtain the values for the three key parameters. The results and discussion are presented in section 4.

2. THE GENERAL CONCEPT AND EQUATION

The X-ray radiation of young and middle-aged SNRs is usually dominated by thermal emission from forward-shocked ISM and reverse-shocked ejecta which are separated by a contact discontinuity. Under strong shock conditions, the thickness of the shocked ISM is about $R/12$ with R as the radius of the SNR. This is sufficiently large that, for a typical SNR, it is possible to measure the elemental abundances of the shocked ISM without any pollution from shocked ejecta with a high spatial-resolution telescope, e.g. *Chandra*.

Suppose one element, X , in the preshock ISM has an abundance of X_{LMC} . The measured postshock gas abundance of element X , from the shock front to contact discontinuity, is X_{po} , and the depletion factor of this element, D_X , is defined as the logarithm of its reduction factor below the expected abundance relative to that of hydrogen if all of the atoms were in the gas phase (Jenkins 2009):

$$D_X = \text{Log}[N(X)/N(H)] - \text{Log}(X/H)_{\text{LMC}}, \quad (1)$$

in which $N(X)$ is the column density of X in gas phase and $N(H)$ is the column density of hydrogen. Finally, we have the expression:

$$X_{\text{po}} = X_{\text{LMC}} \times 10^{D_X} + R_X \times (1 - 10^{D_X}) \times X_{\text{LMC}}. \quad (2)$$

At the right side of Equation 2, the first part is the preshock gas abundance for element X and the second part presents the abundance for the same element returned to gas phase.

The fraction of dust destroyed, R_X , is given by

$$R_X = \frac{X_{\text{po}} - 10^{D_X} \times X_{\text{LMC}}}{X_{\text{LMC}} \times (1 - 10^{D_X})}. \quad (3)$$

As is shown above, we can obtain R_X if we have the values for X_{po} , X_{LMC} and D_X . In the next section, we will introduce how to measure these key parameters.

3. THREE KEY PARAMETERS

3.1. The postshock gas abundances, X_{po}

The postshock gas abundances, X_{po} , are taken from Schenck et al. (2016) where the authors carried out an abundance study of 16 LMC SNRs. By making a three-color map and investigating the literature for each SNR, they selected several small and/or thin regions in the outermost boundary of each SNR for which X-ray radiation is from the shocked ISM. The regions used for spectral fits are shown in their Figure 1. Each region contains at least ~ 3000 counts to allow statistically significant spectral model fits. A nonequilibrium ionization plane-parallel shock model, *vpshock*, with two foreground absorption components from the Milky Way

and LMC, is used to fit the X-ray spectra. They then averaged these measured abundances for each SNR and listed them in their Table 2, with 90% confidence level uncertainties. It's worth noting that, in the definition of X_{po} , the postshock region is defined as the region from shock front to the contact discontinuity. The 'three-color map' method used by Schenck et al. (2016) should naturally guarantee that the regions in their paper contain the whole postshock region. In cases where it might not, the measured X_{po} value will be less than the true value and R_X will be underestimated according to equation (3).

3.2. The ISM abundances of LMC, X_{LMC}

The chemical composition of HII regions has long been used to reference ISM abundances. However, previous studies demonstrated that several heavy elements such as Mg, Si, and Fe show significant depletions in HII regions (Esteban et al. 1998). Another long-standing unsolved issue for HII regions is that the derived abundances depend on both the fluctuations of the electron temperature throughout the nebula and the lines used in the analysis, i.e. the recombination or collisionally excited lines (Peimbert 2005). These make the abundances of HII regions unsuitable for our study. Red giant branch stars can also be used to study ISM abundances. Unfortunately, they belong to the old stellar population and therefore are not good tracers of present-day ISM abundances (Lapenna et al. 2012). An alternative class of objects to provide ISM abundances is that of the slowly-rotating early B-type stars. Unlike HII regions, their composition is not affected by elemental depletions. Considering the fact that they are young and have clean photospheres without strong stellar winds or pollution from convection (no evidence was found for effects of rotational mixing up to projected rotational velocities of 130 km s^{-1} , e.g. Korn et al. 2005), the B-type stars form an ideal reference for present-day ISM abundances.

Since little or no abundance variation between cluster members and field stars has been found (e.g. Korn et al. 2000; Rolleston et al. 2002; Hunter et al. 2007, 2009; Turndle et al. 2007), we use both cluster and field B-type stars to reference the LMC ISM abundances. To do this, we collected 69 B-type stars with abundance measurements from different parts of the LMC (6 from Korn et al. 2000, 4 from Korn et al. 2002, 3 from Rolleston et al. 2002, 3 from Korn et al. 2005, 30 from Hunter et al. 2007 and 23 from Turndle et al. 2007). All of them have projected stellar rotational velocities less than 150 km s^{-1} , indicating nearly all of them are slow-rotating stars if the view is not pole-on. In Rolleston et al. (2002), Hunter et al. (2007) and Turndle et al. (2007), the Si abundances measured based on lines from different ionization states are listed separately. Therefore, we calculate the uncertainty-weighted mean Si abundance for each star by:

$$X_{\text{LMC}} = \frac{\sum_{i=1} (W_i X_i)}{\sum_{i=1} W_i}, \quad (4)$$

TABLE 1
THE FRACTION OF DUST DESTROYED FOR 8 SNRS WITH NON-RADIATIVE SHOCK.

Name	Location	Age (yr)	Percent destroyed	Reference
Cygnus Loop	Milky Way	10000	35%	Sankrit et al. 2010
Puppis A	Milky Way	3700	25%	Arendt et al. 2010
N49B	LMC	10900	27%	Williams et al. 2006
0453-68.5	LMC	8700	33%	Williams et al. 2006
N23	LMC	4600	39%	Williams et al. 2006
N132D	LMC	2500	38% - 50%	Williams et al. 2006
DEM L71	LMC	4400	35%	Borkowski et al. 2006
0548-70.4	LMC	7100	40%	Borkowski et al. 2006

with the weight

$$W_i = \frac{1}{\sigma_i^2} \quad (5)$$

where X_i and σ_i are the Si abundance and the associated uncertainty for each ionization state. The uncertainty of the mean is

$$\sigma = \sqrt{\frac{\sum_{i=1} (W_i \sigma_i)^2}{(\sum_{i=1} W_i)^2}} \quad (6)$$

The above three equations are also used to estimate the uncertainty-weighted present-day global ISM chemical abundances of the LMC and we list the result in Table 2.

TABLE 2
ISM ABUNDANCES OF LMC REFERENCED BY SLOW-ROTATING EARLY B-TYPE STARS AND THE AVERAGED POSTSHOCK GAS ABUNDANCES OF 16 LMC SNRS.

Elements	Abundance $[X/H]^a$	
	LMC	SNRs
C	7.62 ± 0.05	-
N	7.39 ± 0.03	-
O	8.35 ± 0.04	8.04 ± 0.04
Mg	7.07 ± 0.04	6.88 ± 0.06
Si	7.13 ± 0.06	6.99 ± 0.11
Fe	7.21 ± 0.08	6.84 ± 0.05

^a: Abundances are expressed as $[X/H] = 12 + \text{Log}(X/H)$.
Notes: The confidence level is 90%.

3.3. The depletion factor, D_X

As shown in equation (1), the depletion factor, D_X , can be used to describe how much of element X is peeled off from the gas form and locked up into other forms (mainly in the form of dust grains). Previous works showed that different elements usually have different D_X values, and the overall strengths of depletions of many elements differ along different lines of sight (e.g., Jenkins et al. 1986; Crinklaw et al. 1994). It has been also noted that the depletion factor is correlated with the average volume density of hydrogen along each sight line (e.g. Savage & Bohlin 1979). However, those works were carried out for each element independently without a systematic treatment of the relative depletions of the elements. Jenkins (2009) solved this problem by introducing a new parameter called the depletion strength factor, F_* , which represents how far the depletion processes have progressed collectively for all elements in any given case. Then the

depletion factor for different elements can be given by a simple linear relation in a two-parameters form

$$D_X = D_{X,0} + A_X F_* \quad (7)$$

or a three-parameter form

$$D_X = B_X + A_X (F_* - z_X), \quad (8)$$

where $D_{X,0}$ and A_X in Equation (7) are the zero point and slope respectively. In equation (8), the zero point reference for F_* is z_X , which is unique to element X, and B_X is the depletion at that point. For the Milky Way, Jenkins (2009) also found that F_* is linearly correlated with logarithmic volume density $n(\text{H})$

$$F_* = 0.772 + 0.461 \log \langle n(\text{H}) \rangle \quad (9)$$

which means we could give an estimate of the local D_X for each element if we knew the local volume density. Unfortunately, for the LMC, there is no F_* - $\log n(\text{H})$ relation because the distance scale that the LMC neutral gas occupies is unknown, making it nearly impossible to convert column density to volume density. Therefore, we can't estimate the D_X value for each individual LMC SNR even if the local volume density can be derived by fitting their X-ray spectra. But it is still possible to obtain an averaged D_X value for 16 SNRs.

The most recent knowledge about elemental depletions in the LMC is from Tchernyshyov et al. (2015). We rechecked the star sample used by these authors. According to the positions of the stars on the LMC HI column density map (see their Figure 1) and the measured gas column densities for each stars (see their Figure 7), we found no obvious space-distribution bias (e.g., preference for star formation regions or the most diffuse ISM) in their sample. Furthermore, the ISM surrounding LMC SNRs shows even higher dust-to-gas ratios than the averaged ratio of the LMC (Temin et al. 2015). Therefore, it should be safe and maybe somewhat conservative to take the averaged depletion factors in Tchernyshyov et al. (2015) as the elemental depletions for 16 LMC SNRs used in our study.

The depletion factor of an element depends on the ISM total abundance (gas plus dust). Comparing our LMC ISM abundances with the abundances used by Tchernyshyov et al. (2015), there are differences of 0.22 and 0.11 for Si and Fe respectively. We use both values to correct the Si and Fe depletion factors in Tchernyshyov et al. (2015) and obtain the averaged depletion factors of -0.60 and -1.28 for Si and Fe. This indicates that, on average, 75% of Si and 95% of Fe are

locked in dust grains.

4. RESULT AND DISCUSSION

4.1. The averaged fraction of dust destroyed

With the averaged depletion factors, LMC ISM abundances and postshock abundances in hand, now we can calculate the fraction of dust destroyed for the 16 SNRs with equation 3. The results are reported in Table 3. As can be seen, the fraction of Si-rich dust grains destroyed for each SNR is usually higher than the value for Fe rich dust grains. The averaged fraction of destroyed Si-rich dust grains is $61_{-11}^{+16}\%$ while it is only $40_{-1}^{+5}\%$ for Fe rich dust grains. The 21% difference is illustrated clearly in Figure 1 with the 61% destruction dashed line well above most of the data points for Fe.

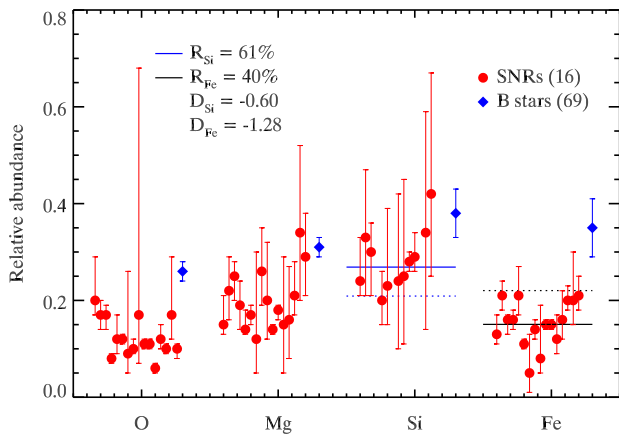


FIG. 1.— The comparison between the postshock gas abundances of 16 SNRs and ISM abundances referenced by early B-type stars. The reference solar abundances are taken from Anders & Grevesse (1989). The red points show the measured postshock abundances of the 16 LMC SNRs and the blue diamonds are the LMC ISM abundances traced by 69 B-type stars. D_{Si} and D_{Fe} represent the depletion factors of Si and Fe. The R_{Si} and R_{Fe} stand for the averaged fraction of destroyed Si-rich and Fe-rich dust grains which are illustrated as solid blue and black lines respectively. In addition, the dotted blue and black lines mark the predicted postshock relative abundances assuming that 40% Si-rich dust grains and 61% Fe-rich dust grains are destroyed.

Moreover, 4 SNRs in our sample have previous fractional dust destruction measurements by Williams et al. (2006) and Borkowski et al. (2006), as shown in Table 1. Adopting the previous value of fractional destruction, we predict the postshock gas abundances and compare them with the abundances from fitting the X-ray spectra in Figure 2. The mismatch between the predictions and measurements for Si are obvious which means that the fraction of dust destroyed that is estimated in our work is higher than previous ones. It is worth noting that Williams et al. (2006) and Borkowski et al. (2006) found the dust to gas mass ratio is lower by a factor of ~ 4 than the typical value calculated by Weingartner & Draine (2001) for the LMC. Williams et al. (2006) explained this discrepancy by suggesting that the dust grains are porous which can reduce the preshock dust content and enhance the sputtering rate. Here, we demonstrate that, with our result, the

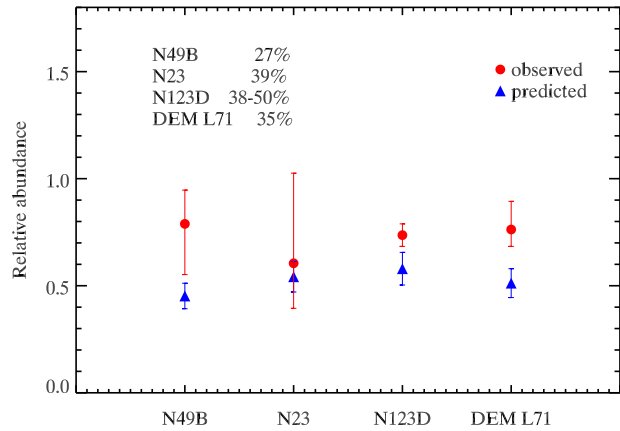


FIG. 2.— The comparison between predicted postshock Si abundances and measured Si abundances relative to LMC Si abundance referenced by slow rotating early B-type stars. The blue triangles are the predicted postshock abundances using previous published fraction of dust destroyed listed in Table 1. The remaining symbols and labels have the same meaning as Figure 1.

discrepancy can be explained naturally without the assumption of porous dust grains. In the Weingartner & Draine (2001) dust model for the LMC, the Si abundance is assumed to be $1.67 \times 10^{-5} H^{-1}$ in dust grains which lead to a dust to gas mass ratio of 2.5×10^{-3} . However, the Si abundance in dust grains is only $1.35 \times 0.75 \times 10^{-5} = 1.01 \times 10^{-5} H^{-1}$ referenced by B-type stars. If the abundances of other elements are reduced by the same amount, the dust to gas mass ratio will decrease to $(1.01/1.67) \times 2.5 \times 10^{-3} = 1.53 \times 10^{-3}$. With the postshock dust to gas mass ratio of about $(1/4) \times 2.5 \times 10^{-3}$ from Williams et al. (2006), the fraction of destroyed dust will be $1 - (0.25 \times 2.5 \times 10^{-3}) / (0.61 \times 2.5 \times 10^{-3}) = 0.6$. This value is consistent with our measurement of $61_{-11}^{+16}\%$.

4.2. Interstellar Fe and its depletion pattern

The abundance of Fe is nearly comparable to Si and Mg (see Table 2). This makes Fe an important component of interstellar dust, especially for the warm neutral medium considering that Fe has a larger depletion factor than Si and Mg. Interstellar olivine ($Mg_2xFe_{2-2x}SiO_4$) or pyroxene ($Mg_xFe_{1-x}SiO_3$) provides possible candidates for Fe (e.g., Mathis et al. 1977). However, according to Poteet et al. (2015), the silicate grains are Mg-rich rather than Fe-rich, suggesting that most of the Fe is in other forms. Since the destroyed fraction of dust inferred by Fe is smaller than the value from Si, our work supports the Poteet et al. (2015) result. The above facts raise two questions. First: “Where is the interstellar Fe?” Potential reservoirs include iron oxides (Henning et al. 1995), iron sulfides (Kohler et al. 2014), and metallic iron (Schalen 1965; Draine & Hensley 2013). Since insufficient amounts of iron oxides and iron sulfides has been detected (Croat et al. 2005; Davis 2011) and metallic iron has been found in different places of the Solar System (Bradley 1994; Westphal et al. 2014; Altobelli et al. 2016), metallic iron is the most likely candidate.

The second question about Fe is how to explain its

TABLE 3
THE FRACTION OF DUST DESTROYED OF 16 LMC SNRS FOR SI-RICH AND FE-RICH DUST GRAINS.

Name	Si	Percent destroyed	Fe	Percent destroyed
SNR		%		%
N63A	$0.24^{+0.09}_{-0.03}$	46	$0.13^{+0.04}_{-0.03}$	36
N49	$0.33^{+0.14}_{-0.12}$	81	$0.21^{+0.03}_{-0.03}$	61
N49B	$0.30^{+0.06}_{-0.09}$	69	$0.16^{+0.01}_{-0.03}$	45
0453-68.5			$0.16^{+0.02}_{-0.02}$	45
0540-69.3	$0.20^{+0.06}_{-0.05}$	30	$0.21^{+0.06}_{-0.04}$	61
N23	$0.23^{+0.16}_{-0.08}$	42	$0.11^{+0.01}_{-0.01}$	30
N157B			$0.05^{+0.08}_{-0.04}$	11
N206	$0.24^{+0.18}_{-0.14}$	46	$0.14^{+0.02}_{-0.02}$	39
DEM L316B	$0.25^{+0.20}_{-0.14}$	50	$0.08^{+0.11}_{-0.03}$	20
N132D	$0.28^{+0.02}_{-0.02}$	61	$0.15^{+0.01}_{-0.01}$	42
DEM L71	$0.29^{+0.05}_{-0.03}$	65	$0.15^{+0.01}_{-0.01}$	42
DEM L238			$0.12^{+0.05}_{-0.03}$	33
0519-69.0	$0.34^{+0.25}_{-0.20}$	85	$0.16^{+0.06}_{-0.04}$	45
0534-69.9	$0.42^{+0.25}_{-0.17}$	-	$0.20^{+0.03}_{-0.02}$	58
0548-70.4			$0.20^{+0.10}_{-0.05}$	58
Honeycomb			$0.21^{+0.04}_{-0.03}$	61
Average	$0.28^{+0.04}_{-0.03}$	61^{+16}_{-11}	$0.15^{+0.01}_{-0.01}$	40^{+5}_{-1}

Notes: Column (2) and (4) are the abundances relative to solar (Anders & Grevesse 1989).

depletion pattern – much higher depletion of Fe in the warm neutral medium compared with Si. As shown in Figure 11 of Tchernyshyov (2015), the solid-phase Fe abundance is roughly constant and always larger than 90% of the total Fe abundance, while the solid-phase Si abundance changes by a factor of about 2 from the least depleted case to the most depleted case. Potential explanations are that the Fe-rich dust grains are either (1) particularly resilient to survival in interstellar shocks or (2) have a very fast regrowth rate even in the diffuse ISM.

Jones et al. (2013) developed a new dust model with a power-law distribution of small amorphous carbon grains and log-normal distributions of large amorphous silicate and carbon grains, which can naturally explain the infrared to far-ultraviolet extinction and other observable dust emission and absorption features. In their model, the answer to the first question is that 70% of Fe exists as the metallic inclusions of amorphous silicate grains. Zhukovska et al. (2018) adopted this value in their analytic dust evolution model which includes different residence times of dust grains and dependence of dust growth on the density and temperature of the gas. By further assuming the remaining 30% Fe is in the form of free-flying metallic nanoparticles, along with a steady state between dust destruction and production by stellar sources and dust regrowth in ISM, they found that the second question can be answered if the 70% metallic inclusion Fe is protected from rapid shock destruction. A direct inference of the Zhukovska et al. (2018) model is that the fraction of Fe-rich dust destruction should be much smaller than 30% because 70% of Fe dust are protected by the silicate grains from shock destruction. If we assume the fraction of destroyed free-flying Fe nanoparticles has the same value as Si-rich dust grains, then the actual fraction of Fe-rich dust destruction is $\sim 18\%$ which is less than half of the measured value of

$40^{+5}_{-1}\%$. Therefore, our result supports that the high depletion of Fe in diffuse neutral medium is not caused by the resilience of Fe rich grains, but its fast growth even in diffuse ISM.

4.3. Comparison with the abundances of O and Mg

The results of Poteet et al. (2015) indicate that nearly all of Mg is in the silicate dust grains in the line of sight of ζ Oph. If it is also true for the LMC diffuse ISM, we expect that the amount of Si and Mg returned to gas phase should be similar. Unfortunately, we can not find the depletion factor of Mg in the literature to calculate the amount of Mg returned to gas phase by equation $X_{po} - X_{LMC} \times 10^{D_x}$. If we assume the amount of Mg released from the dust grains is 70% of the value of Si (Poteet et al. 2015), then we need $\sim 26\%$ of Mg in the gas phase for the preshock ISM. This is a reasonable value if the depletion patterns (the slope) of Mg are similar in both Milky Way and LMC.

The problem arises from the oxygen. Assuming the silicate dust is in the form of olivine or pyroxene, then the amount of released O should be 3 or 4 times larger than Si. If all the solid O is in silicate dust grains, we need more than $\sim 62\%$ of O in solid phase which is much higher than the predicted value (Jenkins 2009; Draine 2015). The discrepancy may be explained in the light of:

(1) Solid O is not all in the form of silicate grains. Micrometer-sized H_2O ice grains could be an important reservoir of the missing O without violating the observational constraints (Wang et al. 2015). However the destruction timescale of H_2O ice grains is short, ($n_e t \sim 10^7 \text{ cm}^{-3} \text{ s}$), which makes H_2O an inappropriate explanation of the O postshock abundances. Another form to contain part of the missing O may be Fe oxides.

(2) The measured postshock O abundances are not correct. Elemental abundances are determined by line in-

tensities. Strong lines usually have more weight than weak lines during the determination. Resonance line emission is caused by the transition between the ground state and the first energy level of an ion. Resonance line photons can be effectively scattered out of a special line of sight (LOS) to another direction if the ion column density along that LOS is large. Since all the regions used to determine postshock elemental abundances are the limbs of the SNR, the LOS path length is much larger than the path length in the perpendicular direction. Therefore, resonance line scattering can lead to an underestimate of elemental abundances during X-ray spectral fitting. X-ray spectroscopic observations of the Cygnus Loop show that the relative abundance of O is two times smaller than other heavy elements. Miyata et al. (2008) found evidence for resonance line scattering for O VII $K\alpha$ line in the *Suzaku* X-ray spectrum of the Cygnus Loop which can explain 20% to 40% of the difference. So, we need to check whether resonance line scattering is important or not in our sample. Taking N49B as an example, the angular size is $2.6''$ which is equal to a diameter of 38 pc assuming the distance of LMC is 50 kpc. The temperature is 0.52 keV while the ionization timescale is $2.1 \times 10^{11} \text{ cm}^{-1} \text{ s}$. Following Miyata et al. (2008), the line-center cross section of resonance scattering can be expressed as

$$\sigma = 1.86 \times 10^{-9} \frac{f}{E} v^{-1} \text{ cm}^2, \quad (10)$$

where f and v are the oscillator strength and thermal kinetic velocity of the ion. E represents the line-center energy. The line-center optical depth is given by

$$\tau = \left(\frac{n_z}{n_Z} \right) \left(\frac{n_Z}{n_H} \right) \left(\frac{n_H}{n_e} \right) n_e \sigma L, \quad (11)$$

where n_z/n_Z is the ionization fraction, n_Z/n_H is the relative abundance, and n_e is the electron density, L the path length through the plasma. For the O VII $K\alpha$ line, v , f , n_z/n_Z , n_Z/n_H , n_e and L are about 100 km s^{-1} , 0.72, 0.0026, 2×10^{-4} , 1.1 cm^{-3} and 10 pc respectively. So τ is about 1.9×10^{-3} indicating that resonance line scattering is not important for the O VII $K\alpha$ line. However for the O VIII $\text{Ly}\alpha$ line, the oscillator strength is 0.42 and the ionization fraction is about 0.2 from AtomDB¹ which gives $\tau \sim 0.3$. This value is somewhat of an underestimate because most of the photons are emitted in the layer where the O VIII ionization fraction peaks and the ionization fraction is probably more like 0.5 which increases τ to around 0.75. Thus, the apparent low abundance of O might be accounted by resonance scattering of the strongest O lines.

Two other potential reasons that can cause incorrect O abundance estimates are: 1) the energy resolution of ACIS detector is too low to separate different lines in the 0.5 to 1 keV range; 2) one single *vpshock* model may be too simple to fit the X-ray spectrum correctly. If those are the reasons for the unusual O abundances, the real abundance uncertainty of Si and Fe should be larger than what we cited. The next generation X-ray telescopes, such as *Athena*, may help to solve this problem because of their high energy resolution.

HZ and WWT acknowledge support from National Key R&D Program of China(2018YFA0404203, 2018YFA0404202) and NSFC (11603039, U1738125). POS acknowledges support from NASA contract NAS8-03060. The authors thank T. Temim for providing helpful comments after reading a draft version of this article.

REFERENCES

- Anders, E., & Grevesse, N. 1989, *Geochim. Cosmochim. Acta*, 53, 197
- Altobelli, N., Postberg, F., Fiege, K., et al. 2016, *Science*, 352, 312
- Bradley, J. P. 1994, *Science*, 265, 925
- Bocchio, M., Jones, A. P., & Slavin, J. D. 2014, *A&A*, 570, A32
- Borkowski, K. J., Williams, B. J., Reynolds, S. P., et al. 2006, *ApJ*, 642, L141
- Croat, T. K., Stadermann, F. J., & Bernatowicz, T. J. 2005, *ApJ*, 631, 976
- Davis, A. M. 2011, *Proceedings of the National Academy of Science*, 108, 19142
- Dopita, M. A., Seitzenzahl, I. R., Sutherland, R. S., et al. 2016, *ApJ*, 826, 150
- Dopita, M. A., Vogt, F. P. A., Sutherland, R. S., et al. 2018, *ApJS*, 237, 10
- Draine, B. T., & Salpeter, E. E. 1979, *ApJ*, 231, 438
- Draine, B. T. 2003, *ARA&A*, 41, 241
- Draine, B. T. 2009, *Cosmic Dust - Near and Far*, 414, 453
- Draine, B. T., & Hensley, B. 2013, *ApJ*, 765, 159
- Draine, B. T. 2011, *Physics of the Interstellar and Intergalactic Medium* (Princeton, NJ: Princeton Univ. Press)
- Draine, B. T. 2015, *IAU General Assembly*, 22, 2253136
- Dwek, E., Foster, S. M., & Vancura, O. 1996, *ApJ*, 457, 244
- Dwek, E., Galliano, F., & Jones, A. P. 2007, *ApJ*, 662, 927
- Dwek, E., & Cherchneff, I. 2011, *ApJ*, 727, 63
- Gall, C., Hjorth, J., & Andersen, A. C. 2011, *A&A Rev.*, 19, 43
- Henning, T., Begemann, B., Mutschke, H., & Dorschner, J. 1995, *A&AS*, 112, 143
- Hunter, I., Dufton, P. L., Smartt, S. J., et al. 2007, *A&A*, 466, 277
- Hunter, I., Brott, I., Langer, N., et al. 2009, *A&A*, 496, 841
- Jenkins, E. B. 2009, *ApJ*, 700, 1299
- Jones, A. P., Tielens, A. G. G. M., & Hollenbach, D. J. 1996, *ApJ*, 469, 740
- Jones, A. P., Fanciullo, L., Köhler, M., et al. 2013, *A&A*, 558, A62
- Korn, A. J., Becker, S. R., Gummertsbach, C. A., & Wolf, B. 2000, *A&A*, 353, 655
- Korn, A. J., Keller, S. C., Kaufer, A., et al. 2002, *A&A*, 385, 143
- Korn, A. J., Nieva, M. F., Dafon, S., & Cunha, K. 2005, *ApJ*, 633, 899
- Köhler, M., Jones, A., & Ysard, N. 2014, *A&A*, 565, L9
- Lakićević, M., van Loon, J. T., Meixner, M., et al. 2015, *ApJ*, 799, 50
- Lapenna, E., Mucciarelli, A., Origlia, L., & Ferraro, F. R. 2012, *ApJ*, 761, 33
- Maiolino, R., Schneider, R., Oliva, E., et al. 2004, *Nature*, 431, 533
- Mathis, J. S., Rumpl, W., & Nordsieck, K. H. 1977, *ApJ*, 217, 425
- McKee, C. F., Hollenbach, D. J., Seab, G. C., & Tielens, A. G. G. M. 1987, *ApJ*, 318, 674
- Miyata, E., Masai, K., & Hughes, J. P. 2008, *PASJ*, 60, 521
- Poteet, C. A., Whittet, D. C. B., & Draine, B. T. 2015, *ApJ*, 801, 110
- Peimbert, A., & Peimbert, M. 2005, *Revista Mexicana de Astronomia y Astrofisica Conference Series*, 23
- Raymond, J. C., Ghavamian, P., Williams, B. J., et al. 2013, *ApJ*, 778, 161
- Rolleston, W. R. J., Trundle, C., & Dufton, P. L. 2002, *A&A*, 396, 53
- Schalén, C. 1965, *PASP*, 77, 409
- Schenck, A., Park, S., & Post, S. 2016, *AJ*, 151, 161
- Shull, J. M. 1977, *ApJ*, 215, 805
- Slavin, J. D., Dwek, E., & Jones, A. P. 2015, *ApJ*, 803, 7
- Temim, T., Dwek, E., Tchernyshyov, K., et al. 2015, *ApJ*, 799, 158
- Tchernyshyov, K., Meixner, M., Seale, J., et al. 2015, *ApJ*, 811, 78
- Trundle, C., Dufton, P. L., Hunter, I., et al. 2007, *A&A*, 471, 625
- Valiante, R., Schneider, R., Bianchi, S., & Andersen, A. C. 2009, *MNRAS*, 397, 1661

¹ <http://www.atomdb.org/>

Wang, S., Li, A., & Jiang, B. W. 2015, *MNRAS*, 454, 569
Weingartner, J. C., & Draine, B. T. 2001, *ApJ*, 548, 296
Westphal, A. J., Stroud, R. M., Bechtel, H. A., et al. 2014, *Science*, 345,

Williams, B. J., Borkowski, K. J., Reynolds, S. P., et al. 2006, *ApJ*, 652, L33
Zhukovska, S., Henning, T., & Dobbs, C. 2018, *ApJ*, 857, 94